Monolithic perovskite/silicon tandems with >28% efficiency: role of silicon-surface texture on perovskite properties

Michele De Bastiani,[1,6,†,] Rawan Jalmood,[1,†] Jiang Liu,[1,†] Christina Ossig,[2,3] Aleš Vlk,[4] Karol Vegso,[5] Maxime Babics,[1] Furkan H. Isikgor,[1] Anand S. Selvin,[1] Randi Azmi,[1] Esma Ugur,[1] Alessandro J. Mirabelli,[1,7] Erkan Aydin,[1] Thomas G. Allen,[1] Atteq Ur Rahman,[1] Emmanuel Van Kerschaver,[1] Peter Siffalovic,[5] Michael E. Stuckelberger,[2] Martin Ledinsky,[4] Stefaan De Wolf[1,*]*

1 KAUST Solar Center (KSC), Physical Sciences and Engineering Division (PSE), King Abdullah University of Science and Technology (KAUST), Thuwal 23955-6900, Kingdom of Saudi Arabia.
2 Center for X-ray and Nano Science CXNS, Deutsches Elektronen-Synchrotron DESY, Notkestraße 85, 22607 Hamburg, Germany
3 Department Physik, Universität Hamburg, Luruper Chaussee 149, 22761 Hamburg, Germany
4 Laboratory of Nanostructures and Nanomaterials, Institute of Physics, Academy of Sciences of the Czech Republic, v. v. i., Cukrovarnická 10, Prague, 162 00, Czech Republic.
5 Institute of Physics, Slovak Academy of Sciences, Dúbravská cesta 9, 845 11 Bratislava, Slovakia
6 current affiliation: Department of Chemistry & INSTM Università di Pavia, Via T. Taramelli 14, Pavia 27100, Italy
7 current affiliation: Department of Chemical Engineering & Biotechnology, University of Cambridge, Philippa Fawcett Drive, Cambridge CB3 0AS, United Kingdom.
* Email: Michele.debastiani@kaust.edu.sa Stefaan.dewolf@kaust.edu.sa
† These authors equally contributed to this work.

Abstract (150 words)

Textured silicon wafers as used in silicon solar cell manufacturing offer superior light trapping, which is a critical enabler for high-performance photovoltaics. A similar optical benefit can be obtained in monolithic perovskite/silicon tandem solar cells, enhancing the current output of the silicon bottom cell. Yet, such complex silicon surfaces may affect the structural and optoelectronic properties of the overlying perovskite films. Here, through extensive characterization based on optical and microstructural spectroscopy, we find that the main effect of such substrate morphology lies in an altering of the photoluminescence response of the perovskite, which we associate with thickness variations of the perovskite, rather than lattice strain or compositional changes. With this understanding we rationalize the design of high-performance perovskite/silicon tandems, yielding certified power conversion efficiencies of >28%.

Keywords

Perovskite photovoltaics; perovskite-silicon tandem solar cells; silicon texturing; current matching; silicon heterojunction solar cells

Introduction

In the last few years, research on perovskite/silicon tandem solar cells has rapidly progressed, already achieving now certified power conversion efficiencies (PCEs) beyond 29%.[1] This surge in device performance underlines the great promise this technology holds to take a future leading role in the photovoltaic (PV) market.[2] However, one of the major challenges for true commercial success is to find alignment with existing industrial practices of manufacturing, in terms of methods and materials, to guarantee competitiveness with mainstream single-junction crystalline silicon (c-Si) PV technology.[3] Monolithic perovskite/silicon tandems may be built from silicon sub-cells with an atomically polished front side. This type of configuration enables a relatively easy translation of the state-of-the-art labscale processing for single-junction perovskite solar cells – which typically still relies on spin-coating of precursor solutions – to tandem technology.[1b-d, 4] Yet, any contemporary commercial c-Si solar cell features a textured front surface.[5] For most devices this texture consists of random pyramids, resulting from alkaline etching of monocrystalline as-cut Si(100) wafers.[6] The resulting texture forms an almost-ideal geometric-optics light trapping system and also reduces front reflection losses, thereby increasing current generation and the PCE on device level.[7] Moreover, the mechano-chemical process to polish c-Si surfaces comes at a prohibitive cost for large-scale PV manufacturing.[4] This mandates the search for perovskite deposition methods compatible with the textured nature of the c-Si bottom cell, as commonly used in industry. To this end, Shali *et al*., followed by Aydin *et al.,* developed a hybrid deposition process to form conformal perovskite layers on textured c-Si

surfaces.[7] Later, Hou *et al.* and Chen *et al.* also realized efficient tandems by covering textured c-Si bottom cells with a solution-deposited perovskite film.[1a, 8] Such solution deposition, for instance in the form of low-cost and scalable slot-die coating, is of high appeal for translation to industry.[9] Moreover, these processes can benefit from the large know-how that is already available for single-junction perovskite solar cells.[10] Finally, Roß *et al.* explored vacuum-based co-evaporation of perovskite films on textured substrates.[11] Overall, these works have focused mostly on empirically developing and optimizing perovskite deposition processes towards efficient tandems. Yet, the true understanding of the influence of textured substrates on the crystallization and material properties of the deposited perovskite is far from complete. Yet, improving our insight in this topic is critical to reach the ultimate process design of tandem devices, merging excellent optical design with outstanding optoelectronic properties of the involved photovoltaic absorbers and interfaces. In this direction, we investigate here the impact of the c-Si surface morphology on the optoelectronic properties of the overlying perovskite absorbers grown from solution, and investigate correlations with device performance. First, we studied via advanced characterisation in depth the differences between perovskite films deposited on flat and textured c-Si substrates. Subsequently, we narrowed our investigation on the impact that different wafer texturing processes have on the optoelectronic properties and the performances of tandems. Building on this knowledge, we provide evidence for the optimal conditions and processing and validate our findings by fabricating 28.1% efficient perovskite/silicon tandem solar cells, featuring a c-Si bottom-cell with optimal texture for tandem applications.

Results and discussion

Texturing the surface of c-Si wafers with alkaline solutions is a well-established process in the c-Si PV industry. The process is based on the etching of silicon atoms along the [100] crystallographic direction due to the lower binding energy compared to the [111] crystallographic direction.[6, 12] This results in the formation of randomly distributed pyramids with a uniform size, depending on the processing conditions. These pyramids reduce the front reflection of the incoming light and form an excellent light trapping system, increasing the current output of the device.[13] In the tandem configuration, the texturing favors the current matching of the two sub-cells towards higher values, boosting the overall device performance.[7] However, the deposition of the perovskite film on the textured c-Si surface from solution is not trivial and the optoelectronic properties of the film itself significantly differ from those on flat substrates. Figure 1a shows the distribution of the photoluminescence (PL) emission of the $Cs_{0.05}MA_{0.14}FA_{0.81}Pb(I_{0.8}Br_{0.2})_3$ perovskite film deposited on flat and textured c-Si substrates. The same perovskite composition shows two different emission spectra with an apparent shift in the peak position: ~1.65 eV on the textured substrate and ~1.67 eV on the flat substrate. Moreover, the PL distribution is narrower on the textured substrate than on the flat. This difference is also present in the distribution of the Urbach energy (E_U, see Figure S1), where smaller values suggest less disorder and a higher electronic quality for the perovskite deposited on the textured c-Si wafer.[14] To elucidate the origin of the PL shift, we performed crystallographic and elemental analysis on the two samples. The grazing-incidence wide-angle X-ray scattering (GIWAXS, Figure S2) patterns of the perovskite deposited on textured and flat substrates do not present significant variations, indicating that the morphology of the substrate does not alter the crystallographic

properties. To investigate the potential effect of a strain induced by the textured substrate,[15] we performed temperature-dependent PL spectroscopy (see Figure S3). Indeed, in presence of a different lattice strain between the flat and textured sample, we expected a different shift of the PL signals with temperature. However, the blue-shift in the PL at higher temperature is found to be similar for both samples (~0.03 eV), suggesting that the difference in the optical properties is not strain-induced. Further, we monitored the elemental distribution in the two films via spatially resolved X-Ray fluorescence (XRF) microscopy (Figure 1b). We used the lead (Pb) distribution as a fingerprint for morphological control. The Pb distribution matches well the pyramid distribution for the textured sample, with a lower signal at the tips where the film is thinner. Similarly, for the flat sample, the Pb distribution resembles the micron-scale wrinkled structure which is typical of triple cation perovskite films incorporating Cs^+.[16] Interestingly, the wrinkled structure is observed as an additional modulation on top of the morphological variation induced by the c-Si surface structure. The distribution of iodide (I) and bromide (Br) follows the thickness variation of Pb, which leads to an overall homogeneous I/Br ratio, although we have observed spots with locally lower I/Br ratio that coincide with the tips of the textured samples. To further investigate the origin of the PL shift, we deposited Br-free perovskite films with two different compositions (triple cation, $Cs_{0.05}MA_{0.14}FA_{0.81}PbI_3$; and methylammonium lead iodide, $MAPbI_3$) on flat and textured c-Si substrates. In both cases, the PL of the flat substrates blue-shifts, similar to the mixed halide composition (Figure 1c). This directly excludes the halide distribution as the only origin of the PL shift. On the other hand, the XRF measurements in Figure 1b suggest that the film thickness can affect the optoelectronic properties of the perovskite, particularly for films deposited on textured c-Si, wherein the film reaches a thickness above 1µm. Therefore, we

fabricated $Cs_{0.05}MA_{0.14}FA_{0.81}Pb(I_{0.8}Br_{0.2})_3$ perovskite films with two different thicknesses, 900 nm and 250 nm respectively, on flat substrates. Even in this case the PL differs for the two samples (Figure S4): the PL emission of the thick sample is centered at ~1.65 eV, while the emission of the thin sample is centered at ~1.67 eV. This suggests that for the thicker sample the emitted photons have higher reabsorption probability, which in the end shifts the PL spectrum to lower energies [29]. Moreover, the light-trapping induced by the c-Si pyramidal surface effectively increases the length of the phonon path in the perovskite film, causing an analogous reabsorption effect. In view of tandem integration, we may conclude that the optoelectronic properties of the perovskite film are strongly influenced by the morphology of the bottom cell. This is particularly evident in the influence on the optical thickness of the perovskite film, which shifts the PL emission without altering the bandgap of the perovskite.[17]

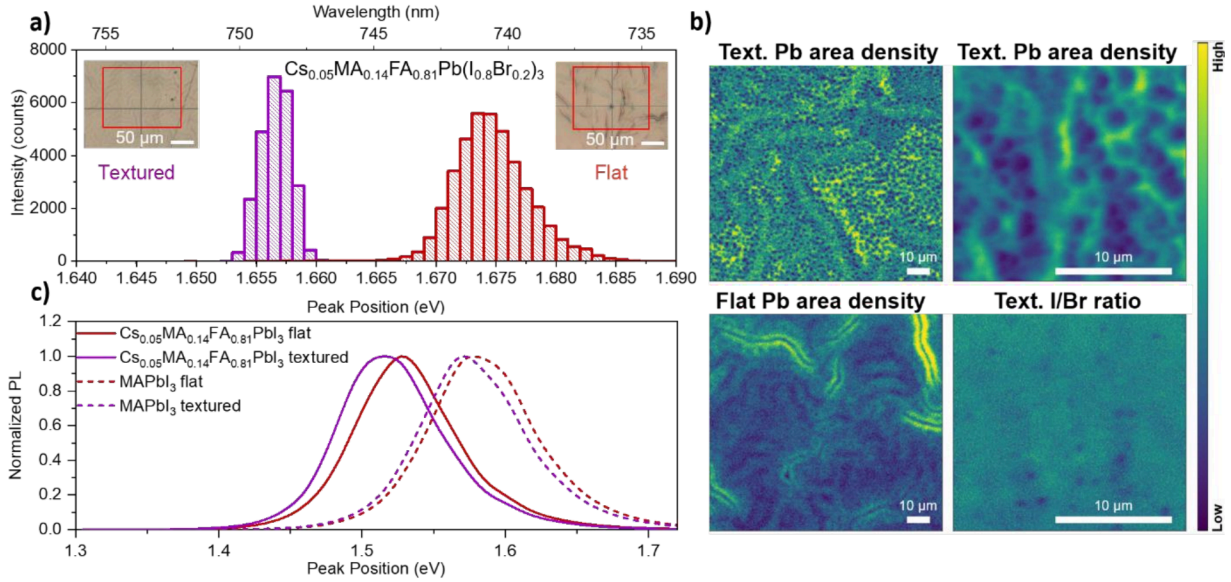

Figure 1. Optoelectronic properties of perovskite films on textured and flat substrates. a) Statistical distribution of the PL emission of a triple cation perovskite film on textured (purple) and flat (red) silicon substrates. The optical microscopy image of the samples with the probed areas are reported in the inset. b) Elemental mapping of triple cations perovskite films on flat and textured substrates from scanning XRF measurements. On the left, Pb distribution as morphological fingerprint of the perovskite film on textured and flat Si. On the right, zoom of an area on the textured sample with the Pb and I/Br distribution. c) PL emission of iodide-only perovskite films (triple cation $Cs_{0.05}MA_{0.14}FA_{0.81}PbI_3$ solid line, and $MAPbI_3$ dashed line) on textured (red) and flat (black) silicon substrates.

Silicon texturing is since decades a standard process in every c-Si PV technology, both for multi- and monocrystalline wafers. Despite its widespread industrial application, little is reported on the parameters that govern the texturing process, and most of the expertise remains within industry. While different approaches can be used to texture the surface of monocrystalline silicon, as used for all high-efficiency c-Si solar cells, alkaline etching represents the simplest yet most effective procedure among many. In this process, c-Si wafers are immersed in alkaline solutions (either using KOH or NaOH, often adding IPA or commercial additives to improve the uniformity) at a specific temperature and for a specific amount of time. Figure 2 shows the influence of temperature, time, and potassium hydroxide (KOH %) concentration on the texturing size (represented here by the diagonal of the pyramid's base) evaluated statistically via top view scanning electron microscopy (SEM) images. Increasing the process temperature from 65 °C to 90 °C increased the texturing size from an average of 0.4 to 1.2 µm (Figure 2a). Similarly, a longer processing time increased the texturing size from 0.2 to 1.0 µm (Figure 2b). Further, we investigated the role of the KOH concentration in water by keeping the temperature and processing time constant. Even in this case, we noted that the texturing size increased from 0.6 to 2 µm by increasing the KOH concentration from 0.75% to 2.89% (Figure 2c). For each of the above conditions, we characterized the weighted reflectance of the textured wafers. Figure 2d shows the reduction of the weighted reflectance from 28% to 15%, by increasing the temperature of the texturing bath. Similarly, Figure 2e shows the reduction of the weighted reflectance from 29% to 13% by increasing the texturing time from 5 to 20 min. In this case of KOH concentration change, the weighted reflectance showed a minimum trend with optimal conditions reached at ~3% of KOH for a weighted reflectance of 13.5% (Figure 2f). In light of these results, we

determined four different processes to texture c-Si wafers for tandem application with different texturing sizes: 0.5 μm (sample A), 1 μm (sample B), 2 μm (sample C) and 5 μm (sample D). For the fabrication details, we refer to the *Methods* section. We used samples A to C to evaluate the performance of the silicon heterojunction (SHJ) bottom cells, as used in this study. The devices used here as bottom cells mainly differ from a conventional solar cell by their top contact; here, the top contact features a layer that has been optimized to serve as a recombination junction, rather than an optimized transparent electrode, as would be common for single-junction SHJ solar cells. These devices are further optimized towards bottom cell application by maximizing their current output in the IR region and the FF at 0.5 Suns (corresponding to the effective operational conditions in tandem application), sacrificing the performance in the visible region (which is anyway taken care of by the perovskite top cell). Figure 2g shows the figures-of-merit of SHJ bottom cells with different texturing sizes, tested under standard AM1.5 1 Sun conditions. We found that the texturing process of sample B yielded the best device performance. The short-circuit current density (J_{SC}) is the lowest (31 mA/cm^2) for sample A and increases for the others (35 and 34 mA/cm^2 for samples B and C, respectively). The lowest current in sample A is in line with a high weighted reflectance and with the fact that for such small texturing, several regions of the wafer feature non-textured areas (see Figure S5). We noted that the open-circuit voltage (V_{OC}) remains largely unaffected by the pyramid size. Indeed, all the samples showed similar values around 715 mV. The fill factor (FF) resembles the similar trend of the J_{SC}, with 71%, 78% and 75% for samples A, B, and C, respectively. Combined together, sample B achieved the highest PCE (19.5%), followed by sample C (18.5%, and then sample A (16%). Figure 2h shows the external quantum efficiency (EQE) and 1-reflection of the SHJ bottom cells. Even in this case, it is clear

that sample A presents high reflection losses over the whole spectrum, which limits the device current.

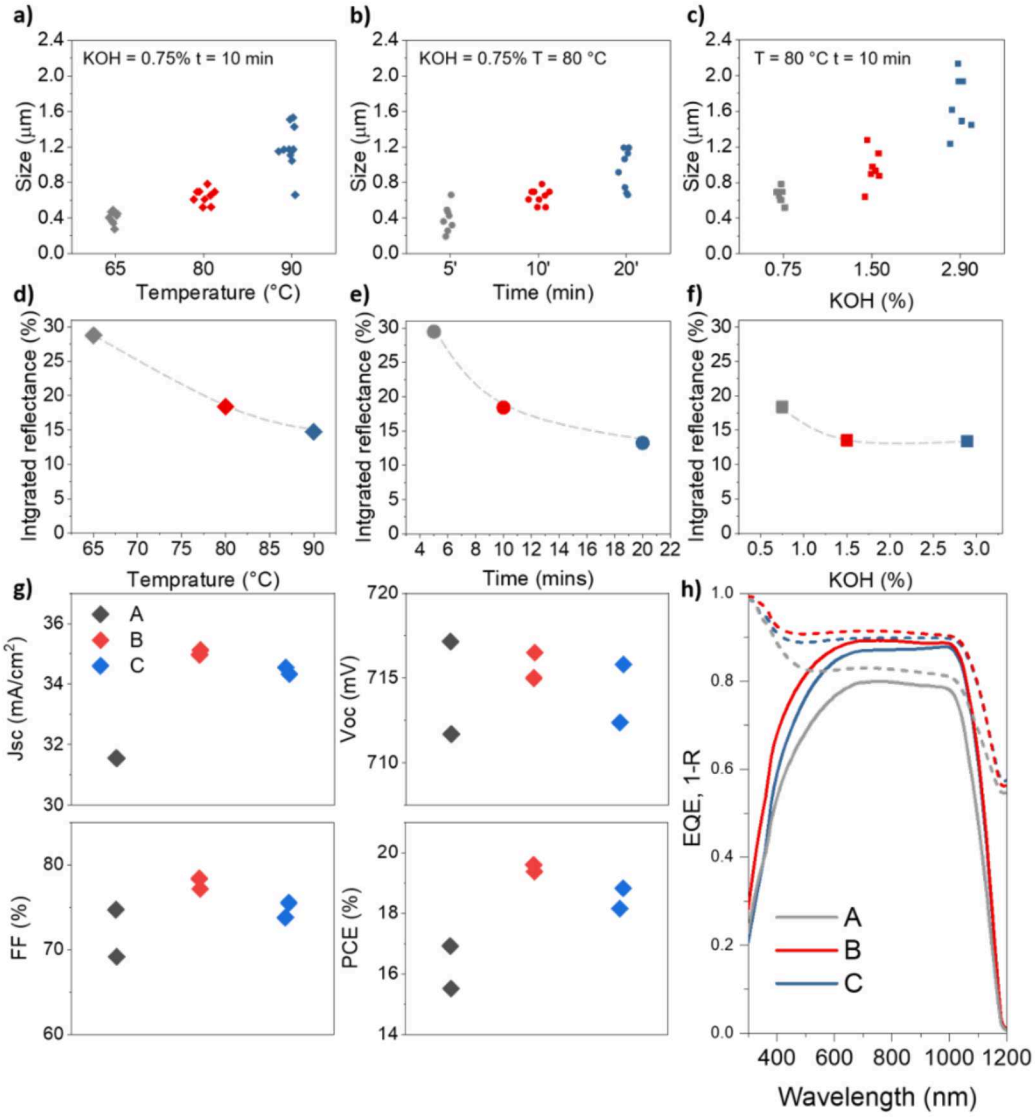

Figure 2. Texturing process of silicon wafers and bottom cell performances. a), b), c) Influence of temperature, time, and KOH concentration on the pyramid sizes, respectively. The other two fixed parameters are reported in the inset of the graphs. d), e), f) Integrated reflectance of silicon wafers as a function of temperature, time, and KOH concentration. g) Figures of merit of silicon heterojunction bottom-cells fabricated on textured wafers with different pyramid sizes. The devices employ as a top contact the ITO recombination junction layer. h) EQE and 1-R of the devices with different texturing process.

Once we determined the role of texturing on the PCE of the bottom cell, we focused on understanding how different pyramid sizes can affect the perovskite performance. Figure S6 shows a schematic illustration of the perovskite spin-coating process onto the SHJ bottom-cell.

With this process, we aim to obtain perovskite films that cover the textured sub-cell uniformly and without pinholes. Therefore, the perovskite thickness needs to be adjusted according to the texturing size.[1a, 9c, 18] To do so, we prepared a concentrated perovskite solution (1.7 M) to obtain micrometer-thick films.[19] Importantly, these films present a high level of crystallinity with mostly single uniform grains over the whole thickness of the film, as shown in the cross-sectional SEM images of samples A, B, and C (Figure 3a). However, when the texturing size exceeded 2 µm (sample D, see Figure S7) the perovskite film presents pinholes where the tip of pyramids emerged from the film. Subsequently, we used hyperspectral PL imaging to collect the emission properties on each point of the perovskite films deposited on the three different textured c-Si wafers (A-C). Figures 3b-c show that there is a correlation between the PL emission and the morphology of the films.[20] Indeed, we extrapolated the intensity profiles from the PL maps (Figure 3d) and noted that sample A presents similar features of the perovskite film deposited on flat substrates (Figure 1), with the typical wrinkles due to the cesium (Cs) content.[16] These wrinkles appear to have a stronger PL signal than other flat regions. Sample B shows features that resemble those of sample A, but less intense and more distributed. Sample C appears uniform both in the morphology and the emission. Similar to what we reported in Figure 1a, even here the PL of the three samples is peaked at different energies: at higher energies sample A, than sample B, and finally C (Figure 3e). Even if this shift is less pronounced than that reported on flat substrates, it clearly correlates the effect of substrate texture with the optoelectronic properties of the perovskite film as used for tandems. To get enhance insight into the optical properties of the three samples, we used time-resolved photoluminescence (TR-PL) spectroscopy (Figure 3f). Interestingly, the TR-PL dynamics are different for the three samples, with sample A

that presents the fastest decay, followed by sample B, and C with the longest. From the bi-exponential fit of the transients, we calculated an average carrier lifetime of 20.6 ns for sample A, 39.9 ns for sample B, and 50.3 ns for sample C. This trend matches with a similar trend that we found in the TR-PL dynamic of perovskite samples with different thicknesses (see Figure S8), correlating the optoelectronic properties with the thickness of the perovskite film and the morphology of the substrate.

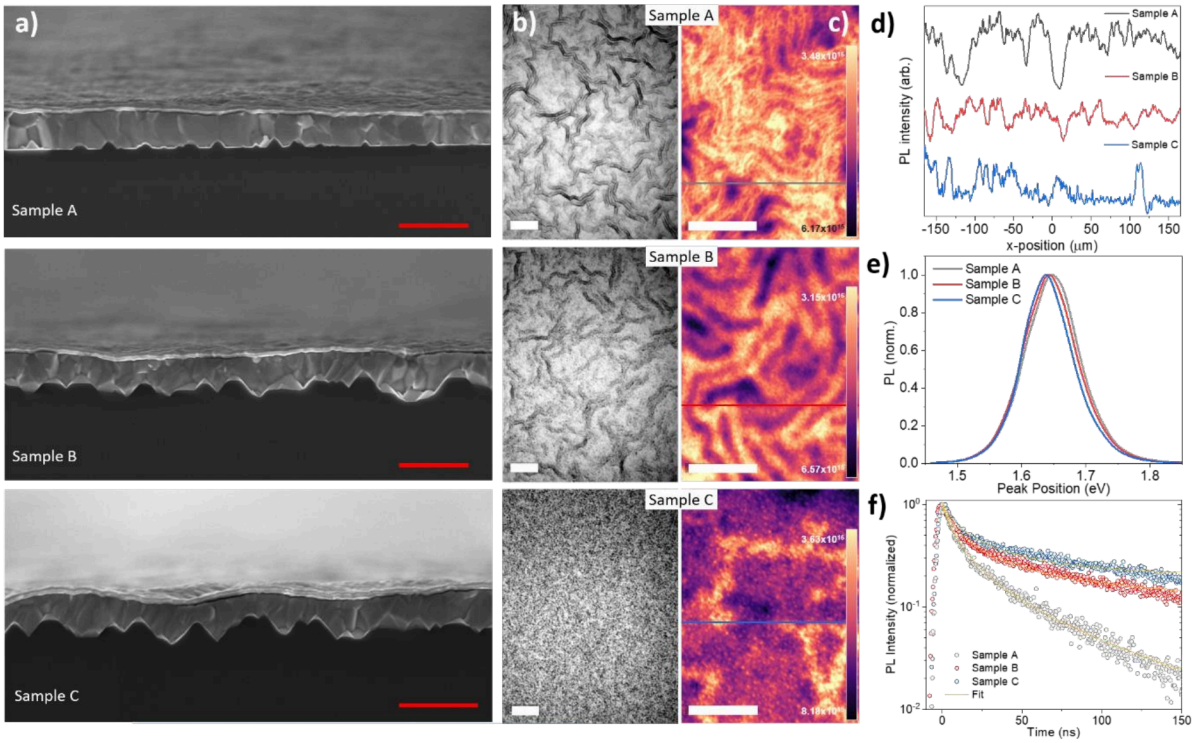

Figure 3: Optoelectronic properties of triple cation perovskite films on silicon substrates with different texturing. a) SEM cross-section images of the perovskite film deposited on sample A, B, and C. The images show the different pyramid sizes due to the different texturing processes. The perovskite film is capped with the top contact for tandem integration. Red scale bar: 2 μm b) Optical microscopy images (black and white) and c) hyperspectral PL imaging (colored) of the three samples. White scale bar: 50 μm. d) PL profile extracted from the hyperspectral images, showing the correlation between the PL intensity and the morphology of the perovskite. e) Averaged PL emission from the probed area of the hyperspectral maps. f) TR-PL dynamics of the three samples. Yellow lines: bi-exponential fitting. All the samples are prepared on textured silicon covered with 100 nm of dielectric insulating layer deposited by low- pressure CVD, to prevent interactions between the perovskite and the silicon.

Next, we realized monolithic perovskite/silicon tandem solar cells using SHJ bottom cells, textured with the same protocols used for samples A, B, and C. Figure 4a shows the tandem layout, while Figure 4b shows the representative current-voltage (*J–V*) curves of the best devices

for the tandems realized on sample A, B, and C (namely tandem A, B, and C). The inset summarizes the figures of merit of the devices. Tandem B and C perform similarly, with a better FF for tandem B resulting in PCE of 28.4% (reverse scan). Overall, the different size of the texturing does not influence the V_{OC}. As expected, in tandem A the higher reflection of the wafer resulted in a lower J_{SC}, even in the presence of the IZO/MgF_2 bilayer anti-reflective coatings. The lack of current is partially compensated with a higher FF, likely due to a current-mismatch condition that enhances the FF.[21] Figure 4c shows the EQE of the tandems and the reflection spectra. Interestingly, the perovskite response (>20 mA/cm^2) is similar for the three devices. This means that the geometrical effect of the texturing does not significantly enhance the current output of the top cell. Likely, the levelized surface of the perovskite film and the efficient absorption of the µm-thick films minimize the optical effect of the texturing. Conversely, this would not be the case of conformal perovskite films, where even the perovskite would benefit optically from the texture.[7, 11, 22] Contrarily, the silicon response is affected by the different texturing. Similar to Figure 2h, the tandem A shows a lower response due to higher reflection losses, which in turn limits the overall current of the tandem. We note that increasing the texturing size slightly increases also the hysteresis in the JV curves. Therefore, we report in Figure 4c independently certified maximum power point (MPP) tracking for tandem B. The certified power output (27.37 mW ± 0.63 mW) corresponds to a PCE of 28.03% under an illumination area of 0.9767 cm^2, in line with our lab findings. This clearly demonstrate that the ideal bottom cell must be sought in light of the tandem configuration, rather than aiming purely at its own record performance. The recent progress of single-junction SHJ technology reached PCEs >26% in both conventional and back-contacted configurations.[23] While these devices represent themselves

an outstanding level of sophistication, such performances are not yet required to achieve record PCEs in tandem configuration. Indeed, as we showed in this work, the performances of the bottom cell must be optimized mainly for their IR response. Simultaneously, the configuration of the bottom cell must be tailored to accommodate the perovskite top cell processing, aiming at high tandem performance. This strategy may come at the cost of sacrificing the visible current-response and reconsidering the texturing process in light of the presence of the perovskite film. For these reasons, the conventional interpretation of the PCE of the bottom cell does not directly correlate with the final efficiency of the tandem.

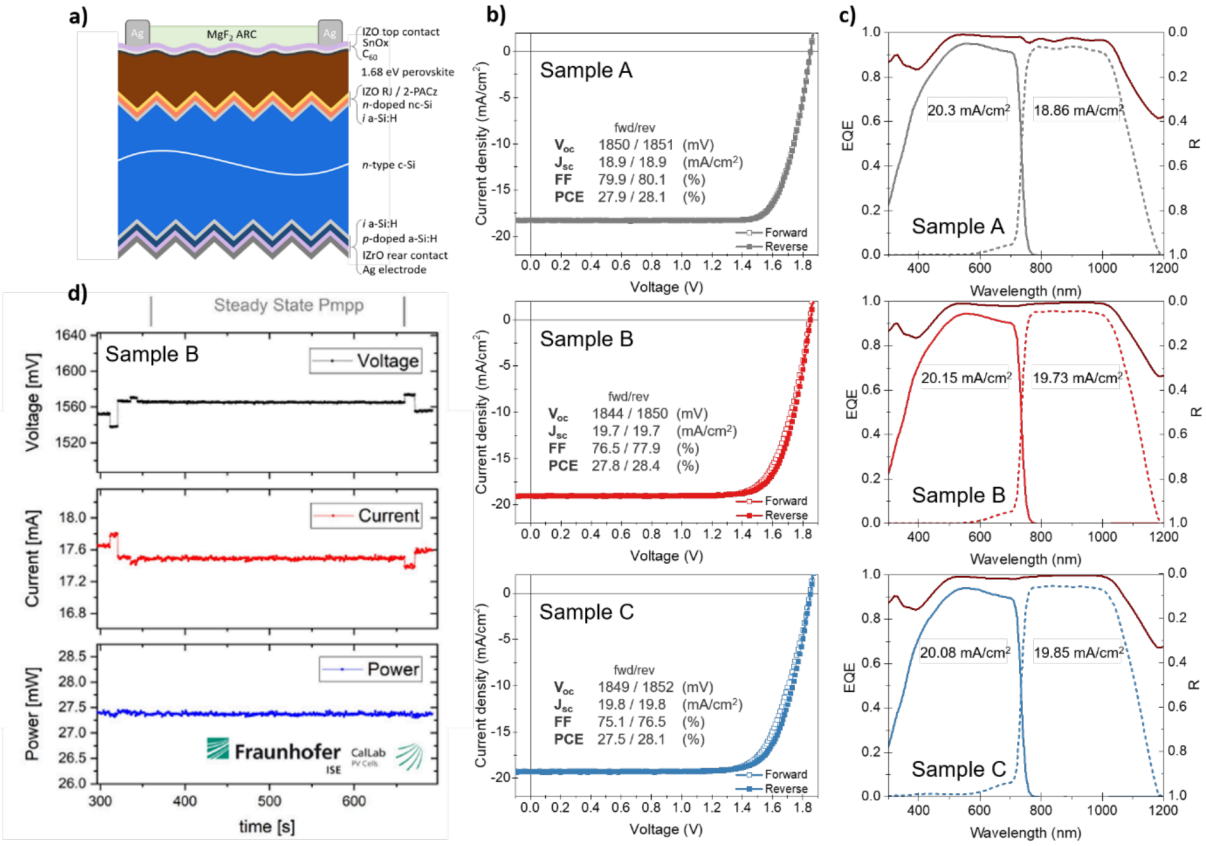

Conclusions

The condition of current matching between the two sub-cells of the tandem is essential to achieve high PCEs. The tuning of the perovskite bandgap is a unique property that gives the perovskite/silicon tandem technology its potential to disrupt the PV market. However, we showed here that the optoelectronic properties of the perovskite are influenced not only by the chemical formulation (a parameter easily controlled in the fabrication process) but also by secondary factors, such as the texturing of the silicon bottom cell and the thickness of the perovskite film itself. In particular, the type of texturing is of paramount importance aiming at performances beyond the 30% PCE threshold. Indeed, the texturing enhances the current generation of the silicon bottom cell, mitigating the need to widen the perovskite bandgap and the variations due to the thickness of the perovskite film. Moreover, the texturing is a well-established process in c-Si PV manufacturing, and can be easily adapted both on solution or vacuum processing of the tandem. In light of our findings, we foresee that both the new generation of high-efficiency perovskite/silicon tandems and the industrial initiative will be established on baseline of textured silicon bottom cells.

Supporting Information

Supporting Information is available from the Wiley Online Library or from the author.

Acknowledgments

We acknowledge the use of KAUST Solar Center and Core Lab facilities and the support from its staff. This work was supported by the King Abdullah University of Science and Technology (KAUST) under award nos. IED OSR-2019-4208, IED OSR-2020-4611, OSR-CRG2019-4093, OSR-CRG2020-4350, OSR-CARF/CCF-3079, REI/1/4833-01-01. We also acknowledge DESY (Hamburg, Germany), a member of the Helmholtz Association HGF, for the provision of experimental facilities. Parts of this research were carried out at PETRA III and we would like to thank Jan Garrevoet, Thomas Sheppard, Mikhail Lyubomirskiy, Martin Seyrich, Thea Engler, Ken Vidar

Falch, and Gerald Falkenberg for assistance in using beamline P06, and Giovanni Fevola and Svenja Patjens for discussions. Beamtime was allocated for proposal II-20190762. M.L. and A.V. acknowledge Czech Ministry of Education, Youth and Sports grant no. CZ.02.1.01/0.0/0.0/16_026/0008382 (CARAT) and the use of the CzechNanoLab research infrastructure supported by the MEYS (LM2018110). P.S. and K.V. acknowledge grant APVV-20-0111 of the Slovak Research and Development Agency.

Experimental Section/Methods

Silicon texturing: The bottom cell (SHJ) was fabricated on float-zone double-polished 4-inches wafers (TOPSIL, n-doped, resistivity 1–5 Ωcm^{-1} and thickness 250–280µm). The texturing process was done in an alkaline solution to obtain randomly textured pyramids. To optimize the pyramids sizes, we started by testing out the three parameters: temperature, time and KOH% using beaker of 2L volume. The three recipes that have been selected for the three samples are: sample A 65 °C, [KOH] = 0.75%, processing 10 min; sample B 80 °C, [KOH] = 0.75%, 20 min; sample C 80 °C, [KOH] = 2.89%, 10 min. To further enhance the etching process, a texturing additive (TS40- Scenergy, 1%) was used to improve the wetting of the solution and to avoid bubbling during the process, which can harmful for the uniformity of the texturing. To obtain texturing sizes bigger than >5 µm, for Sample D, we used a different recipe: 83 °C, [KOH] = 6%, 20 min with a different type of additive (Pure Etch TK81 and TT72C13 from HPC, 0.75% and 0.57% respectively). For each solution, the beaker was placed on a stirring hotplate with a magnetic bar to heat and distribute the solution evenly. After optimizing the conditions for all the samples, we transferred the processes to semi-automatic wet-benches (JST) with heated and circulating baths (25 L volume) for the wafers texturing. After the texturing process, the wafers were thoroughly rinsed in DI water and washed in a solution of KOH/H_2O_2 (60 °C, two min, [KOH] = 0.4%; $[H_2O_2]$ = 1%) to remove the additive leftovers. The wafers were stored for a cleaning process prior to PECVD deposition. The cleaning process is based on the two steps of the RCA procedure with SC1 (NH_4/H_2O_2) and RCA2 (HCl/ H_2O_2), intermediated by dipping in HF (5%) to remove the oxide layer formed.

Tandem fabrication: After the cleaning process, the intrinsic (i) amorphous silicon (a-Si:H) layer was deposited for passivating the wafer surfaces followed by the doped layers (amorphous-p and nanocrystalline-n, 12 and 40nm, respectively) by PECVD in an Octopus2 cluster (Indeotec). On the rear-side, the contact is provided with a stack of sputtered ITO and Ag (110 and 250 nm, respectively); on the front, the recombination junction is provided with 20 nm of sputtered IZO. Both depositions are done in the PVD part of the Octopus cluster

Perovskite deposition and top cell fabrication: The bottom cells are UV-Ozone treated for 15 min to facilitate the anchoring of 2-(9H-Carbazol-9-yl)ethyl phosphonic acid (2PACz), which works as HTL. 2PACz is spin-coated (1 mg/ml in ethanol) and annealed in glovebox. Subsequently, 1.68 eV perovskite $Cs_{0.05}MA_{0.14}FA_{0.81}Pb(I_{0.8}Br_{0.2})_3$ is spin-coated from a 1.7M solution in 4:1 DMF:DMSO and annealed at 100 °C for 15 min. The spin-coating process is shown in the supporting information. Thermally evaporated (Angstrom Engineering) C60 (nanoC), capped by atomic layer deposited SnO2 (Picosun) work as ETL and buffer layer. Finally, 100 nm of IZO are sputtered (Angstrom Engineering) to realize the transparent electrode, while 350 nm of Ag are thermally evaporated to secure the electrical contact. 110 nm of MgF_2 are thermally evaporated as anti-reflective coating.

Characterization: The Hyperspectral photoluminescence (PL) imaging was done using a hyperspectral microscope (Photon etc). The laser excitation at 532 nm is focused through a microscope objective 20x with exposure time of 5s and power 350 W. The perovskite film was protected via encapsulation done in nitrogen glovebox with epoxy resin to prevent humidity exposure. PL mapping was measured on Renishaw InVia Reflex implemented in nitrogen glovebox to protect the sample degradation. Excitation laser 532 nm with intensity comparable with one sun flux was used. The TR-PL measurements were conducted using a high-resolution streak camera system. The excitation beam at 532 nm (HELIOS 532-4-125, Coherent Inc.) with a pulse width of 0.85 ns and a repetition rate of 1 kHz was focused to excite the samples. The associated PL emission was collected by an optical telescope and spectrally and

temporally resolved using a spectrograph (PI Spectra Pro SP2300) and streak camera (Hamamatsu C10910) system. The data were acquired in photon counting mode using the streak camera software (HPDTA). The absorption and reflection spectra of the Si textured wafers were obtained using a Perkin Elmer Lambda 950 UV-vis-NIR spectrophotometer equipped with an integrated sphere Martin PL. The X-ray fluorescence (XRF) maps were obtained at the hard X-ray microprobe endstation of the PETRA III beamline P06 at 13.5 keV using 50 Be Compound Refractive Lenses (CRL).[24] The XRF spectra were recorded with the single-element XRF detector (Vortex) looking at the sample surface at 70 deg relative to the incident beam in continuous scan mode. The 100 µm x 100 µm scans (Figure 2a and 2b) were performed with 200 nm x 200 nm step size and 10 ms dwell time with the incident X-ray beam perpendicularly entering the top cell. The 20 µm x 20 µm scan (Figure 2c and 2d) was performed with 40 nm x 40 nm step size and 50 ms dwell time with the incident X-ray beam entering the top cell at 45°. For the XRF spectrum fitting, PyMca was used.[25] For the performance evaluations of the bottom cell and the tandem cells we used a LED-based solar simulator (Wavelabs). For the EQE we used the LOANA from PVTools. A GIWAXS laboratory system was used to obtain reciprocal space maps of perovskite layers. The system utilized a microfocus X-ray source (Cu Kα radiation) equipped with focusing Montel optics (Incoatec, Germany). GIWAXS patterns were acquired using a Pilatus 200K two-dimensional X-ray detector (Dectris, Switzerland). The distance between the sample and the detector was 86 mm, and the angle of incidence was 1.8°. The scattering patterns were converted to reciprocal spatial coordinates (q_r, q_z), where q_r and q_z are the parallel and perpendicular wavevector transfer components with respect to the sample surface, respectively.

Data availability

All relevant data that support the plots within this paper and other findings of this study are available from the corresponding authors upon reasonable request.

Acknowledgments

M.D.B., R.J., and J.L. equally contributed to this work. This work supported by the King Abdullah University of Science and Technology (KAUST) Office of Sponsored Research (OSR) under award no. OSR-2018-CPF-3669.02, KAUST OSR-CARF URF/1/ 3079-33-01, KAUST OSR-CRG RF/1/3383, and KAUST OSR-CRG2018-3737. We acknowledge DESY (Hamburg, Germany), a member of the Helmholtz Association HGF, for the provision of experimental facilities. Parts of this research were carried out at PETRA III and we would like to thank Jan Garrevoet, Thomas Sheppard, Mikhail Lyubomirskiy, Martin Seyrich, Thea Engler, Ken Vidar Falch, and Gerald Falkenberg for assistance in using beamline P06, and Giovanni Fevola and Svenja Patjens for discussions. Beamtime was allocated for proposal II-20190762. M.L. and A.V. acknowledges Czech Ministry of Education, Youth and Sports grant no. CZ.02.1.01/0.0/0.0/16_026/0008382 (CARAT) and the use of the CzechNanoLab research infrastructure supported by the MEYS (LM2018110). P.S. and K.V. acknowledge grant APVV-20-0111 of the Slovak Research and Development Agency.

Conflict of interest

The authors declare no conflict of interest.

References

[1] a)Y. Hou, E. Aydin, M. De Bastiani, C. Xiao, F. H. Isikgor, D.-J. Xue, B. Chen, H. Chen, B. Bahrami, A. H. Chowdhury, *Science* **2020**, 367, 1135; b)J. Xu, C. C. Boyd, J. Y. Zhengshan, A. F. Palmstrom, D. J. Witter, B. W. Larson, R. M. France, J. Werner, S. P. Harvey, E. J. Wolf, *Science* **2020**, 367, 1097; c)D. Kim,

H. J. Jung, I. J. Park, B. W. Larson, S. P. Dunfield, C. Xiao, J. Kim, J. Tong, P. Boonmongkolras, S. G. Ji, *Science* **2020**, 368, 155; d)A. Al-Ashouri, E. Köhnen, B. Li, A. Magomedov, H. Hempel, P. Caprioglio, J. A. Márquez, A. B. M. Vilches, E. Kasparavicius, J. A. Smith, *Science* **2020**, 370, 1300.
[2] a)C. Kamaraki, M. T. Klug, T. Green, L. Miranda Perez, C. Case, *Applied Physics Letters* **2021**, 119, 070501; b)S. E. Sofia, H. Wang, A. Bruno, J. L. Cruz-Campa, T. Buonassisi, I. M. Peters, *Sustainable Energy & Fuels* **2020**, 4, 852.
[3] M. De Bastiani, M. Babics, E. Aydin, A. S. Subbiah, L. Xu, S. De Wolf, *Solar RRL*, 2100493.
[4] E. Köhnen, P. Wagner, F. Lang, A. Cruz, B. Li, M. Roß, M. Jošt, A. B. Morales-Vilches, M. Topič, M. Stolterfoht, *Solar RRL* **2021**, 2100244.
[5] T. G. Allen, J. Bullock, X. Yang, A. Javey, S. De Wolf, *Nature Energy* **2019**, 1.
[6] a)J. D. Hylton, R. Kinderman, A. R. Burgers, W. C. Sinke, P. M. Bressers, *Progress in Photovoltaics: Research and Applications* **1996**, 4, 435; b)M. Ju, N. Balaji, C. Park, H. T. T. Nguyen, J. Cui, D. Oh, M. Jeon, J. Kang, G. Shim, J. Yi, *RSC advances* **2016**, 6, 49831.
[7] a)E. Aydin, T. G. Allen, M. De Bastiani, L. Xu, J. Ávila, M. Salvador, E. Van Kerschaver, S. De Wolf, *Nature Energy* **2020**, 5, 851; b)F. Sahli, J. Werner, B. A. Kamino, M. Bräuninger, R. Monnard, B. Paviet-Salomon, L. Barraud, L. Ding, J. J. D. Leon, D. Sacchetto, *Nature materials* **2018**, 17, 820.
[8] B. Chen, J. Y. Zhengshan, S. Manzoor, S. Wang, W. Weigand, Z. Yu, G. Yang, Z. Ni, X. Dai, Z. C. Holman, *Joule* **2020**.
[9] a)E. Aydin, J. Liu, E. Ugur, R. Azmi, G. T. Harrison, Y. Hou, B. Chen, S. Zhumagali, M. De Bastiani, M. Wang, *Energy & Environmental Science* **2021**, 14, 4377; b)J. Liu, E. Aydin, J. Yin, M. De Bastiani, F. H. Isikgor, A. U. Rehman, E. Yengel, E. Ugur, G. T. Harrison, M. Wang, *Joule* **2021**, 5, 3169; c)F. H. Isikgor, F. Furlan, J. Liu, E. Ugur, M. K. Eswaran, A. S. Subbiah, E. Yengel, M. De Bastiani, G. T. Harrison, S. Zhumagali, *Joule* **2021**, 5, 1566.
[10] a)M. Degani, Q. An, M. Albaladejo-Siguan, Y. J. Hofstetter, C. Cho, F. Paulus, G. Grancini, Y. Vaynzof, *Science advances*, 7, eabj7930; b)S. Gharibzadeh, P. Fassl, I. M. Hossain, P. Rohrbeck, M. Frericks, M. Schmidt, M. R. Khan, T. Abzieher, B. A. Nejand, F. Schackmar, *Energy & Environmental Science* **2021**, 14, 5875.
[11] M. Roß, S. Severin, M. B. Stutz, P. Wagner, H. Köbler, M. Favin‐Lévêque, A. Al‐Ashouri, P. Korb, P. Tockhorn, A. Abate, *Advanced Energy Materials* **2021**, 11, 2101460.
[12] E. Vazsonyi, K. De Clercq, R. Einhaus, E. Van Kerschaver, K. Said, J. Poortmans, J. Szlufcik, J. Nijs, *Solar energy materials and solar cells* **1999**, 57, 179.
[13] a)A. Alasfour, J. Y. Zhengshan, W. Weigand, D. Quispe, Z. C. Holman, *Solar Energy Materials and Solar Cells* **2020**, 218, 110761; b)S. Manzoor, M. Filipič, A. Onno, M. Topič, Z. C. Holman, *Journal of Applied Physics* **2020**, 127, 063104.
[14] a)M. Ledinsky, T. Schönfeldová, J. Holovský, E. Aydin, Z. k. Hájková, L. Landová, N. Neyková, A. Fejfar, S. De Wolf, *The journal of physical chemistry letters* **2019**, 10, 1368; b)M. Ledinský, A. Vlk, T. Schönfeldová, J. Holovský, E. Aydin, H. X. Dang, Z. k. Hájková, L. Landová, J. Valenta, A. Fejfar, *The Journal of Physical Chemistry C* **2020**, 124, 27333.
[15] D. Liu, D. Luo, A. N. Iqbal, K. W. Orr, T. A. Doherty, Z.-H. Lu, S. D. Stranks, W. Zhang, *Nature materials* **2021**, 20, 1337.
[16] a)A. Bercegol, F. J. Ramos, A. Rebai, T. Guillemot, J.-B. Puel, J.-F. o. Guillemoles, D. Ory, J. Rousset, L. Lombez, *The Journal of Physical Chemistry C* **2018**, 122, 23345; b)K. A. Bush, N. Rolston, A. Gold-Parker, S. Manzoor, J. Hausele, Z. J. Yu, J. A. Raiford, R. Cheacharoen, Z. C. Holman, M. F. Toney, *ACS Energy Letters* **2018**, 3, 1225.
[17] a)M. Wang, K. Wang, Y. Gao, J. I. Khan, W. Yang, S. De Wolf, F. Laquai, *Solar RRL* **2021**, 5, 2100029; b)T. Yamada, Y. Yamada, Y. Nakaike, A. Wakamiya, Y. Kanemitsu, presented at *European Quantum Electronics Conference*, **2017**.

[18] a)M. De Bastiani, A. J. Mirabelli, Y. Hou, F. Gota, E. Aydin, T. G. Allen, J. Troughton, A. S. Subbiah, F. H. Isikgor, J. Liu, L. Xu, B. Chen, E. Van Kerschaver, D. Baran, B. Fraboni, M. F. Salvador, U. W. Paetzold, E. H. Sargent, S. De Wolf, *Nature Energy* **2021**; b)J. Liu, E. Aydin, J. Yin, M. De Bastiani, F. H. Isikgor, A. U. Rehman, E. Yengel, E. Ugur, G. T. Harrison, M. Wang, *Joule* **2021**.
[19] B. Chen, S.-W. Baek, Y. Hou, E. Aydin, M. De Bastiani, B. Scheffel, A. Proppe, Z. Huang, M. Wei, Y.-K. Wang, *Nature communications* **2020**, 11, 1.
[20] E. M. Tennyson, K. Frohna, W. K. Drake, F. Sahli, T. Chien-Jen Yang, F. Fu, J. Werner, C. Chosy, A. R. Bowman, T. A. Doherty, *ACS Energy Letters*, 6, 2293.
[21] M. Boccard, C. Ballif, *ACS Energy Letters* **2020**, 5, 1077.
[22] Y. Li, B. Shi, Q. Xu, L. Yan, N. Ren, Y. Chen, W. Han, Q. Huang, Y. Zhao, X. Zhang, *Advanced Energy Materials* **2021**, 11, 2102046.
[23] a)K. Yoshikawa, H. Kawasaki, W. Yoshida, T. Irie, K. Konishi, K. Nakano, T. Uto, D. Adachi, M. Kanematsu, H. Uzu, *Nature energy* **2017**, 2, 1; b)Longi, 2021.
[24] G. Falkenberg, F. Seiboth, F. Koch, K. V. Falch, A. Schropp, D. Brückner, J. Garrevoet, *Powder Diffraction* **2020**, 35, S34.
[25] V. Solé, E. Papillon, M. Cotte, P. Walter, J. Susini, *Spectrochimica Acta Part B: Atomic Spectroscopy* **2007**, 62, 63.